nature portfolio

https://doi.org/10.1038/s41586-021-03853-0

Supplementary information

Continuous Mott transition in semiconductor moiré superlattices

In the format provided by the authors and unedited

Supplementary information for
"Continuous Mott transition in semiconductor moiré superlattices"

Tingxin Li, Shengwei Jiang, Lizhong Li, Yang Zhang, Kaifei Kang, Jiacheng Zhu, Kenji Watanabe, Takashi Taniguchi, Debanjan Chowdhury, Liang Fu, Jie Shan, Kin Fai Mak

Correspondence to: jie.shan@cornell.edu, kinfai.mak@cornell.edu
These authors contributed equally: Tingxin Li, Shengwei Jiang, Lizhong Li.

1. Valence band alignments in $MoTe_2/WSe_2$ heterobilayers

To show the absence of direct interlayer charge transfer from $MoTe_2$ to WSe_2, we measure the band offset of the heterobilayer by performing optical studies on 60-degree-aligned $MoTe_2/WSe_2$ moiré superlattices. The spin-resolved type-I band alignment at the K valley is shown in Supplementary Fig. S1a. We examine the reflection contrast spectrum near the WSe_2 intralayer exciton resonance as a function of electric field at a fixed filling factor $f = 1$ (Supplementary Fig. S1b). As illustrated in Supplementary Fig. S1a, there are two possible transition pathways in this energy window: 1) the intralayer neutral exciton of the WSe_2 layer (~ 1.69 eV) that does not disperse with electric field, and 2) the interlayer transition from the $MoTe_2$ lower valence band to the WSe_2 upper conduction band that linearly disperses with electric field. The latter is spin-allowed in the 60-degree-aligned sample but not in the 0-degree-aligned sample. The vertical electric field E tunes the valence band offset between the two layers. When the two transition pathways are tuned to near resonance, hybridization occurs and gives rise to an anticrossing feature near $E \approx 0.32$ V/nm. This anticrossing feature has been studied on another TMD moiré material in Ref. [1]. The result here is fully consistent with the reported results. The electric field at the anticrossing is where the $MoTe_2$ lower valence band becomes nearly degenerate with the WSe_2 upper valence band. The slope of the electric field dispersion of the interlayer exciton resonance gives us the dipole moment of the heterobilayer $\frac{\varepsilon_{hBN}}{\varepsilon_{TMD}} et \approx 0.26$ e*nm. Here $\varepsilon_{TMD} \sim 7-8$ and $\varepsilon_{hBN} \approx 3$ are the out-of-plane dielectric constant of the TMD heterobilayer and the hBN, respectively, and $t \approx 0.7$ nm is the interlayer separation between the two TMD layers. Using the measured dipole moment and the anticrossing electric field ($E \approx 0.32$ V/nm), we can determine the upper valence band offset between the two TMD layers. The $MoTe_2$ valence band maximum is about 300 meV above the WSe_2 valence band maximum under zero electric field (versus 220 meV from DFT). The difference remains above 100 meV at the highest electric field examined in the study. Direct interlayer charge transfer is thus not possible. Note that we have used 60-degree-aligned sample to determine the band offset because the interlayer transition mentioned above is spin-forbidden in 0-degree-aligned samples (Supplementary Fig. S1c), in which no anticrossing feature can be observed (Supplementary Fig. S1d). (The result is also fully consistent with Ref. [1].) We do not expect the band offset to be significantly different for the 0- and 60-degree-aligned samples. The measurement of the band offset in the 60-degree-sligned sample is a good approximation of that in the 0-degree-algined sample.

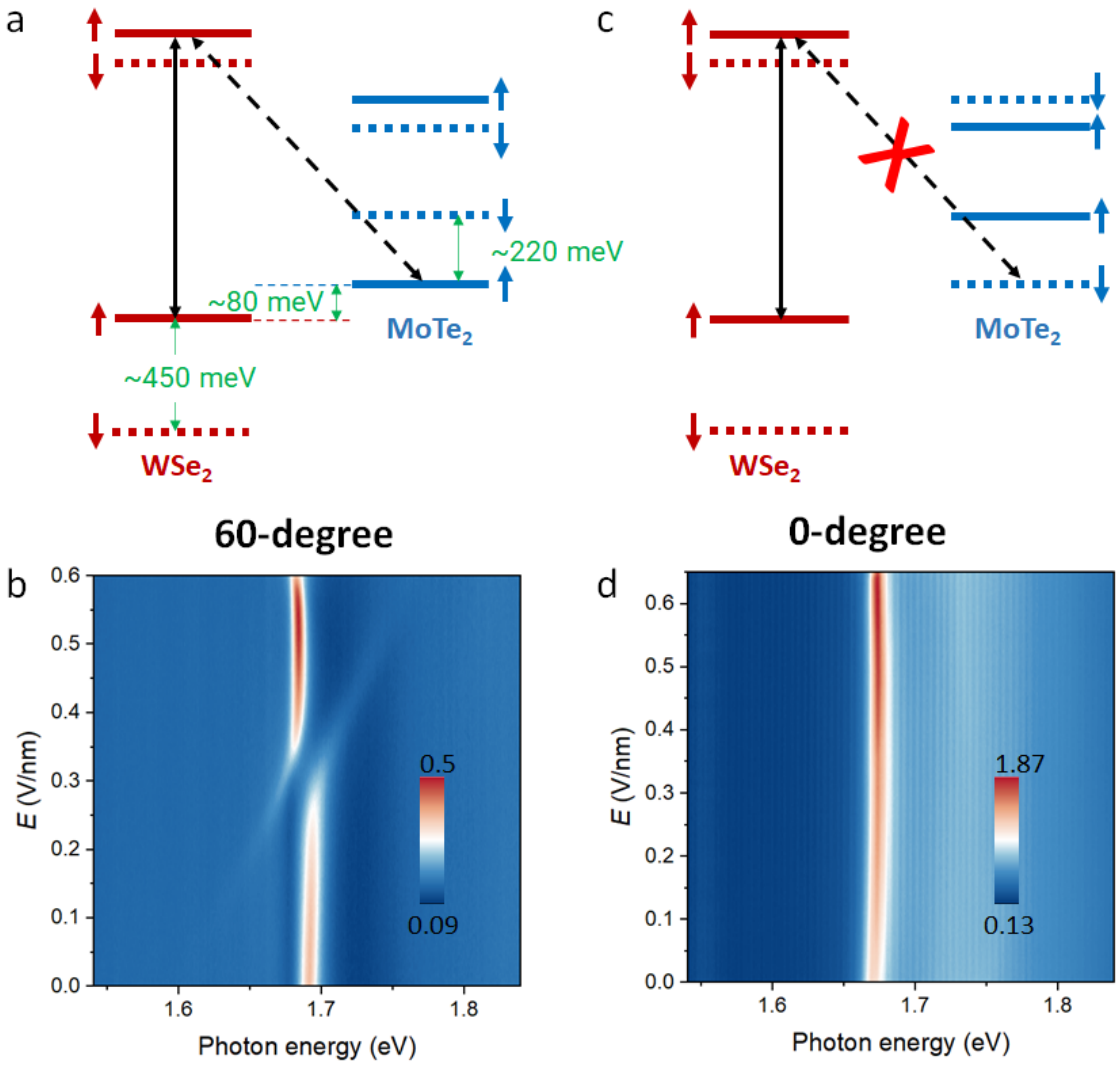

Supplementary Figure S1. Valence band alignments in $MoTe_2/WSe_2$ heterobilayers. **a, c,** Spin-resolved band structure of 60- (**a**) and 0- (**c**) degree-aligned $MoTe_2/WSe_2$ heterobilayers under zero electric field. Dashed and solid double-sided arrows denote the relevant interlayer exciton transition and intralayer exciton transition (the fundamental exciton in WSe_2), respectively, for the spectroscopy measurements. Hybridization of the two transitions is possible when the WSe_2 upper valence band becomes nearly degenerate with the $MoTe_2$ lower valence band. This is allowed only in the 60-degree samples since the two valence bands have the same spins. **b, d,** Optical reflection contrast spectrum near the WSe_2 fundamental exciton resonance as a function of applied electric field at fixed doping density of $f = 1$ in 60- (**b**) and 0- (**d**) degree samples. Hybridization of the intralayer exciton resonance (strong feature that does not disperse with field) and the interlayer exciton resonance (weak feature that disperses linearly with field) is observed in 60-degree samples. A dipole moment of ≈ 0.26 e*nm is determined from the electric field dispersion of the interlayer exciton resonance. The dipole moment allows us to determine the relative band offsets in the heterobilayer as a function of applied electric field.

2. Electric-field-tuned moiré bandwidth

To confirm the existence of bandwidth tuning by the vertical electric field, we perform capacitance measurements on $MoTe_2/WSe_2$ moiré superlattices at varying filling factors and electric fields (see Ref. [2] for measurement methods). Supplementary Fig. S2a shows the differential top gate capacitance as a function of the bottom gate voltage at varying top gate voltages. The top gate capacitance measures the electronic compressibility of the moiré layer [2]. In particular, each capacitance dip corresponds to an incompressible state. In addition to the insulating states at $f = 1$ and $f = 2$, there are also insulating states at $f = 1/3$ and $f = 2/3$, which are generalized Wigner crystal states [3, 4]. As the top gate voltage becomes more negative (i.e. larger electric field at fixed filling factor), the $f = 2/3$ state becomes weaker and eventually disappears while the $f = 1$ and $f = 2$ states remain (we cannot access the $f = 1/3$ state at large negative top gate voltage because of the onset of gate leakage).

The result clearly shows an increase in the bandwidth of the first Hubbard band, which eventually leads to a bandwidth tuned Wigner transition at fixed filling $f = 2/3$. The $f = 2/3$ state is stabilized by the nearest neighbor Coulomb repulsion V (Ref. [3, 4]), which is nearly independent of the electric field. Based on the moiré period ~ 5 nm and the size of the Wannier wavefunction ~ 2-3 nm (Ref. [5]), we estimate $V \sim \frac{U}{2}$. Also, both of the $f = 1$ and $f = 2$ states remain robust at the $f = 2/3$ Wigner transition so that the Hubbard bands remain well separated from each other (Supplementary Fig. S2b). The result is fully consistent with an electric-field-tuned bandwidth W that induces a Wigner transition at $V \sim W$. The bandwidth further increases with electric field and eventually leads to a Mott transition at $f = 1$ at $U \sim W$; the $f = 1$ charge-gap continuously vanishes at the MIT critical point.

Based on the capacitance results, we propose the schematic picture in Supplementary Fig. S2b for the first three Hubbard bands at fixed filling factor of $f = 1$. Because of mixing of the remote moiré bands by the Coulomb interaction, the Hubbard bandwidth increases with the Hubbard band index *f*, consistent with recent studies [2, 4]. With increasing vertical electric field, the $f = 2$ gap closes first, followed by closing of the $f = 1$ gap near the Mott transition. Fortunately, theoretical studies [6, 7] have suggested that the effect of the remote flat bands on the physics near $f = 1$ can be approximated by an effective single-band Hubbard model with renormalized parameters in the Hamiltonian. The situation is similar to that in cuprates [8]. Our experiment is consistent with this view: Extended Data Fig. 1 shows that closing of the $f = 2$ gap at ~ 0.5 V/nm does not perturb the $f = 1$ insulating state, which suggests that the band merging at $f = 2$ does not change the filling factor of the Hubbard band. Otherwise, the MIT at $f = 1$ and $f = 2$ would occur at nearly the same electric field.

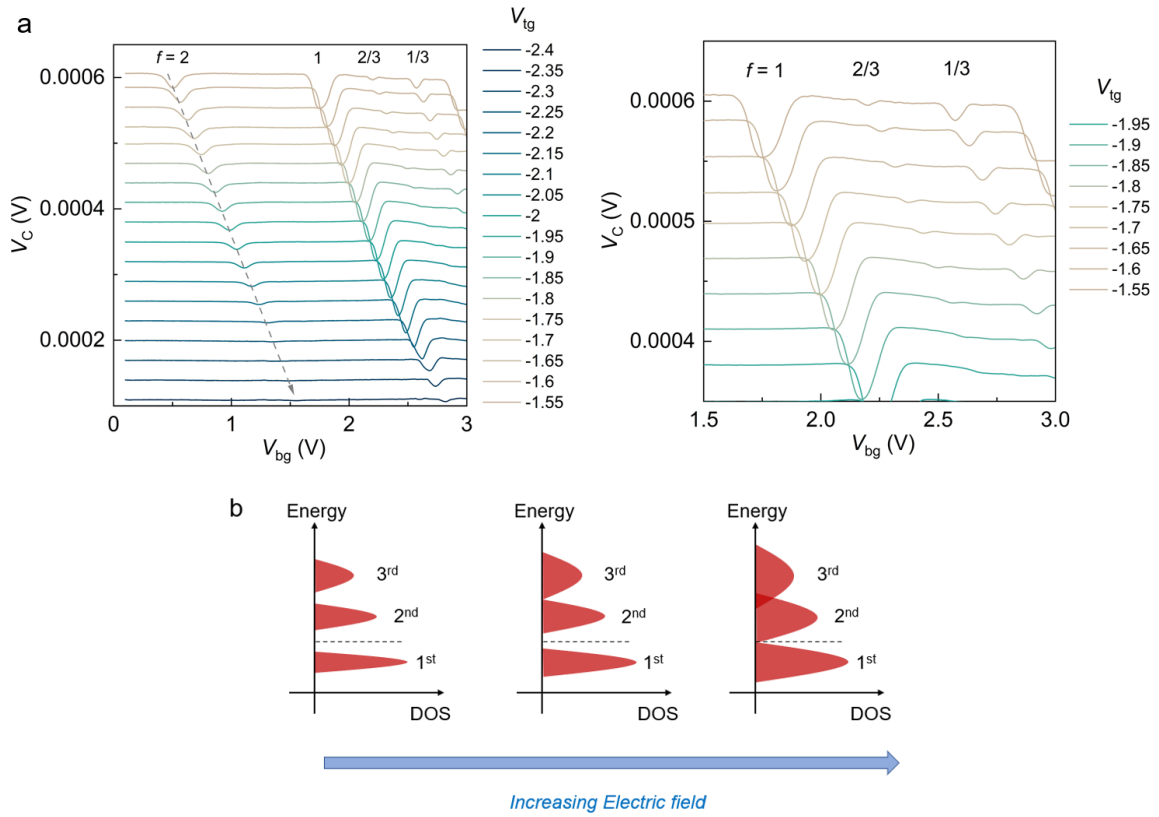

Supplementary Figure S2. Electric-field-tuned moiré bandwidth. a, Differential top gate capacitance as a function of bottom gate voltage at varying top gate voltages ($T = 5$ K). The curves are vertically displaced for clarity. The filling factors of the incompressible states are labeled. The vertical electric field increases along the arrowed dashed lines. The right panel shows more details of the left panel, focusing on the $f = 2/3$ state. **b,** Evolution of the first three Hubbard bands at fixed filling factor of $f = 1$. Because of mixing of the remote moiré bands by the Coulomb interaction, the Hubbard bandwidth increases with the Hubbard band index. With increasing vertical electric field, the $f = 2$ gap closes first, followed by the closing of the $f = 1$ gap near the Mott transition. The closing of the $f = 2$ gap does not change the filling factor of the first Hubbard band to the first approximation.

3. Scaling collapse of resistance curves

For device 1 the first set of measurements was taken down to 1.6 K. It was reloaded into a He-3 insert to measure down to 300 mK in the second set of measurements. The disorder density increased slightly in the second round, which is presumably related to reloading the device and multiple thermal cycles.

Below we include the scaling analysis for both rounds of measurements (separated into two columns in Fig. R3a-h). Figure R3a and R3b show the raw data of $R_{\square}$ versus T in a log-linear plot for varying electric fields. Figure R3c and R3d show the same data in a log-log plot. The critical field and the corresponding resistance $R_C(T)$ are identified from the power-law temperature dependence of resistance (dashed line). In Fig. R3e and R3f

we normalize all the resistance curves by $R_C(T)$ and label them by $E - E_C$. We first rescale the curve furthest from the critical point on the insulating side ($E - E_C$ = -16 mV/nm) by setting $T_0 \approx 220$ K, which corresponds to the gap size determined from the thermal activation fit of $R_\square(T)$ at high temperatures. We determine the value of T_0 for the next normalized resistance curves to best collapse it onto the first curve in Fig. R3g and R3h. Figure R3i shows all the T_0's on the insulating side. We then use the same T_0's to scale the resistance curves on the metallic side with the same $|E - E_C|$ without any adjustment in Fig. R3g and R3h. The values of T_0's from both rounds of measurements show good consistency.

For data from the first round measurements (down to 1.6 K), good collapse of resistance curves can be achieved down to $\sim \pm 1$ mV/nm from the critical point. The collapse starts to fail within $\sim \pm 1$ mV/nm from the critical point presumably due to disorder effects (which broaden the transition as shown in Fig. 1f in the main text). It provides an estimate of the disorder density in the system by using the parallel plate capacitor model $\sim 2\varepsilon_{hBN}\varepsilon_0 \times (1\text{mV/nm}) \sim 5\times 10^{10}$ cm^{-2} ($\varepsilon_{hBN} \approx 3$ is the out-of-plane dielectric constant of hBN and ε_0 is the vacuum permittivity). The disorder density is about two orders of magnitude smaller than the moiré density. For data from the second round of measurements (down to 300 mK), good collapse of curves can only be achieved down to $\sim \pm 2$ mV/nm from the critical point, which corresponds to a higher disorder density $\sim 10^{11}$ cm^{-2}.

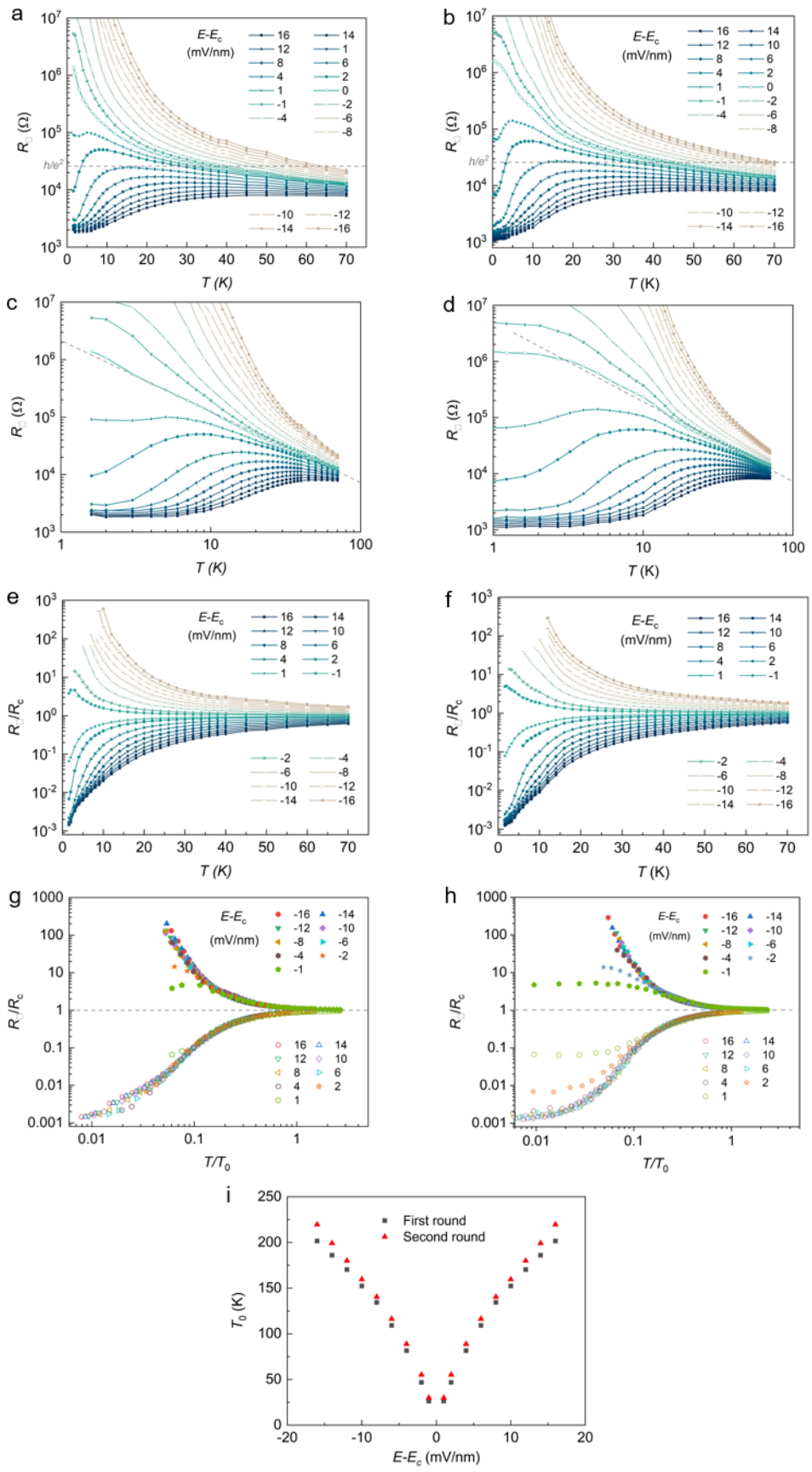
a
b
c
d
e
f
g
h
i
E-E_c (mV/nm)
R_□ (Ω)
h/e²
T (K)
R_□/R_c
T/T_0
T_0 (K)
First round
Second round
E-E_c (mV/nm)

Supplementary Figure S3. Procedures for scaling collapse of resistance curves. a, b, Temperature dependence of square resistance at $f = 1$ under varying electric fields from the first (down to 1.6 K, **a**) and second (down to 300 mK, **b**) round measurements. **c** and **d,** same as **a** and **b**, respectively, in log-log plot. The resistance $R_C(T)$ at $E_C \approx 0.652$ V/nm follows a power-law dependence. **e, f,** Temperature dependence of $\frac{R_\square}{R_C}$ under varying electric fields from the first (**e**) and second (**f**) round measurements. **g, h,** $\frac{R_\square}{R_C}$ versus the scaled temperature $\frac{T}{T_0}$ for selected electric fields for clarity. **i,** Electric field dependence of T_0 near the critical point from the two rounds of measurements.

4. Curie-Weiss analysis

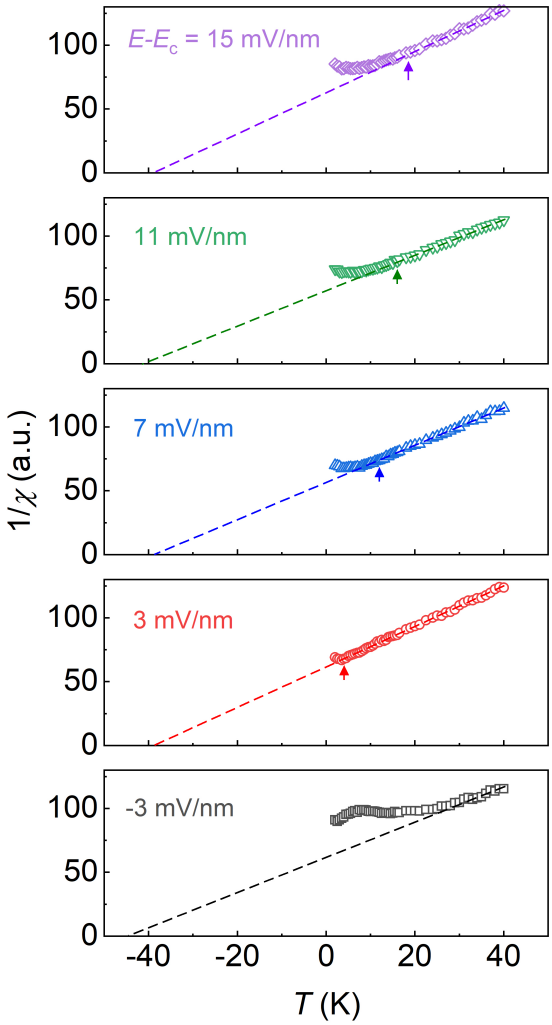

Supplementary Figure S4. Curie-Weiss analysis in the high-temperature limit. Temperature dependence of the inverse magnetic susceptibility χ^{-1} at different electric fields and Curie-Weiss fits (dashed lines) in the high-temperature limit. The obtained Curie-Weiss temperature is ~ 40 K and is weakly dependent on electric field.

5. Additional control experiments on MCD

Supplementary Fig. S5 compares the MCD measurement (1.6 K) of a $WSe_2/MoTe_2$ moiré superlattice at filling $f = 1$ and $E - E_C = 3$ mV/nm (Supplementary Fig. S5a, b) and a charge neutral monolayer of WSe_2 (Supplementary Fig. S5c, d). We show the fundamental exciton spectrum of WSe_2 in two systems under left (black) and right (red) circularly polarized light excitation in Supplementary Fig. S5a, c, and the MCD spectrum in Supplementary Fig. S5b, d. The exciton spectrum in the moiré superlattice red shifts and becomes more complex compared to that in the monolayer. (Due to multiple interference, the absolute reflection contrast depends on the exact distance of the sample from the silicon substrate, which acts as a mirror; it is not meaningful to compare the absolute value.) The excitons in the two systems also respond to the applied magnetic field with opposite sign. We track the MCD at the low-energy peak/dip (vertical dashed lines) as a function of magnetic field (Supplementary Fig. S5e, f). While the magnetic response is linear with field in the monolayer, it increases linearly with field at small fields, saturates above ~ 2 T, and shows a weak linear decrease with field above saturation in the moiré superlattice. The observed linear magnetic response for monolayer TMDs, corresponding to the exciton valley Zeeman effect, is consistent with the literature [9]. The magnetic saturation at a few Tesla is characteristic of local moments. The weak linear reduction in MCD with field above the saturation manifests the contribution of the bare exciton and can be subtracted as a background. The results are fully consistent with Ref. [10], which has also employed magneto-optical measurements to probe the local moments in similar TMD moiré systems.

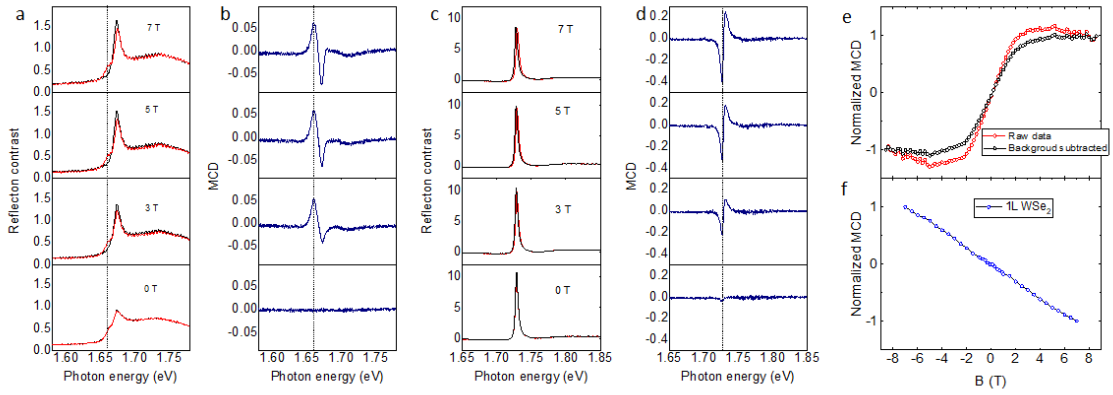

Supplementary Figure S5. Magneto-optical reflection contrast spectrum and MCD spectrum. a,c, Reflection contrast spectrum of left- and right-handed polarized light for $MoTe_2/WSe_2$ moiré sample (**a**) and monolayer WSe_2 (**c**) under several representative magnetic fields. The spectrum focuses on the WSe_2 fundamental exciton resonance. The moiré sample is at $f = 1$ and under 3 mV/nm above the critical field. The WSe_2 sample is charge neutral. **b,d,** MCD spectrum obtained from **a** and **c** for $MoTe_2/WSe_2$ moiré sample (**b**) and monolayer WSe_2 (**d**). **e,f,** MCD response as a function of magnetic field for $MoTe_2/WSe_2$ moiré sample (red, **e**) and monolayer WSe_2 (**f**) at the low-energy

peak/dip of the MCD spectra. The black curve in **e** is obtained after subtracting a linear background from the raw data (red).

The low-temperature magnetic saturation field B^* obtained from the MCD measurement is also independent of the probing wavelength. In Supplementary Fig. S6 we compare B^* from the MCD measurement with the saturation field from the transport measurement on the metallic side. They are largely consistent. The result supports that the MCD probes the magnetic response of the moiré material. We note that here B^* is determined at 85% of the saturated MCD value. Because of the smooth magnetic field dependence for the MCD, it is generally harder to determine B^* from the MCD and the error bars are bigger.

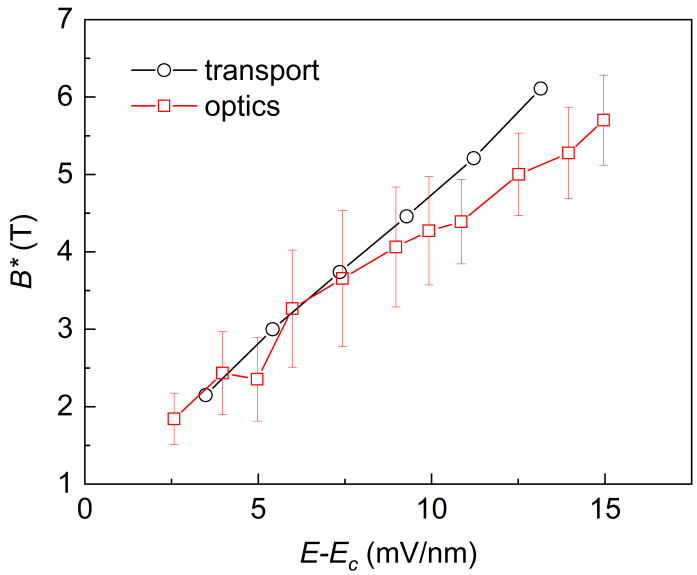

Supplementary Figure S6. Magnetic saturation field versus electric field. Electric-field dependence of the saturation magnetic fields B^* on the metallic side obtained from transport (black) and MCD (red) measurements. The two are in reasonable agreement.

Finally, we show the MCD measurements at several representative electric fields near the critical field on both sides at a fixed magnetic field of 3 T. Supplementary Fig. S7a shows the left- (black) and right-handed (red) reflection contrast spectrum; Supplementary Fig. S7b shows the MCD spectrum obtained from Supplementary Fig. S7a. We choose to probe the system at the low-energy peak, which stays unchanged in wavelength across the MIT. The results justify the use of a single wavelength to probe the magnetic response from the local moments near the MIT.

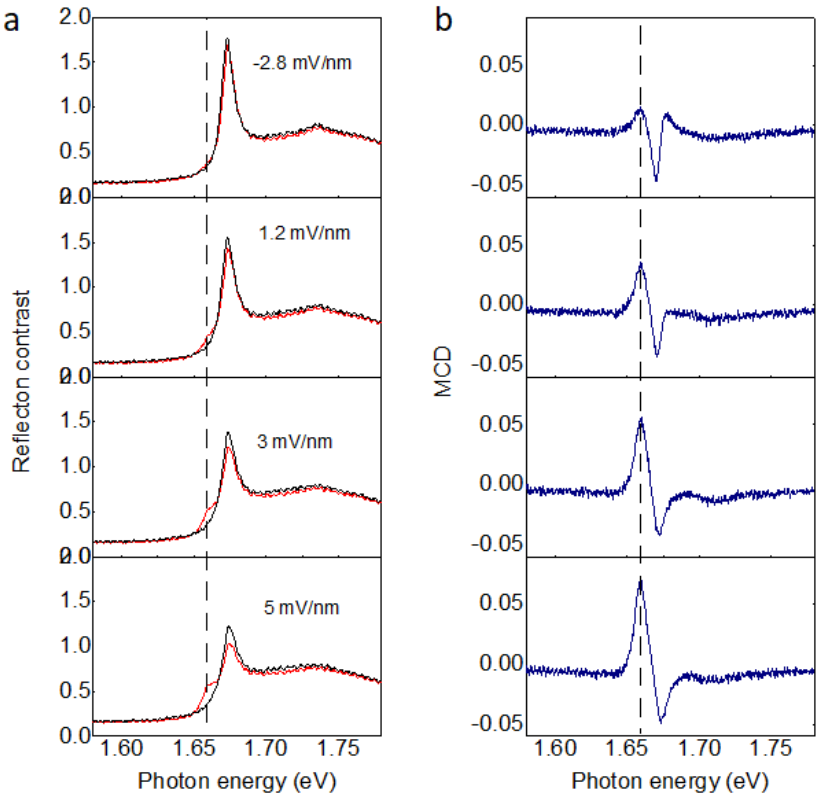

Supplementary Figure S7. Electric field dependent MCD spectrum at 3 T. a, Reflection contrast spectrum at 3 T for the $MoTe_2/WSe_2$ moiré sample at $f = 1$ under several representative applied electric fields. Both left-handed (black) and right-handed (red) polarized spectra are shown. **b,** MCD spectrum obtained from **a**. A clear MCD enhancement near the WSe_2 neutral exciton resonance is observed. Although the amplitude changes, the resonance does not shift with electric field near the MIT critical point. It justifies the use of a single wavelength to probe the magnetic response near the critical electric field.

6. Characterization of sample alignment angle by second-harmonic generation (SHG)

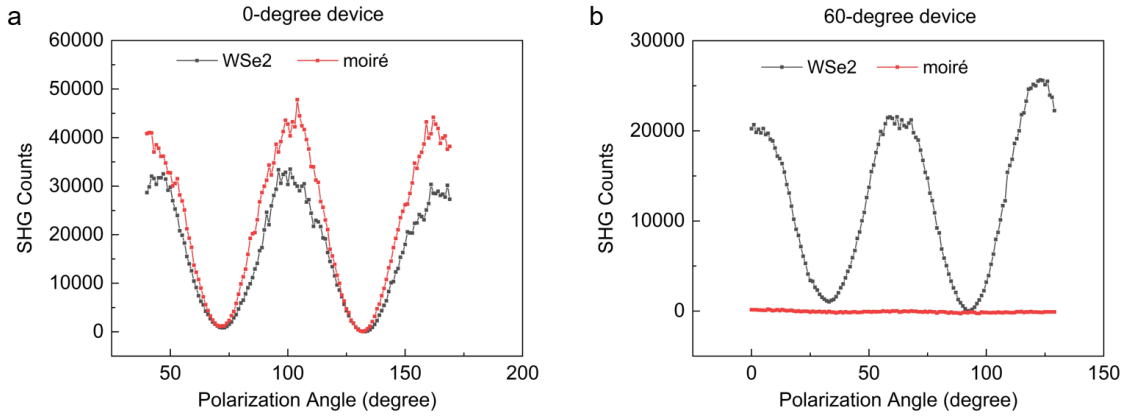

Supplementary Figure S8. Characterization of sample alignment angle by SHG. a,b, Second-harmonic intensity as a function of the polarization angle of the excitation light from 0-degree (**a**) and 60-degree (**b**) $MoTe_2/WSe_2$ heterobilayers. Samples are excited by linearly polarized light under normal incidence. The cross-polarized component of the second harmonic emission is detected. The second-harmonic emission from each monolayer is added constructively in the 0-degree sample (**a**) and destructively in the 60-degree sample (**b**).

7. DFT band structures

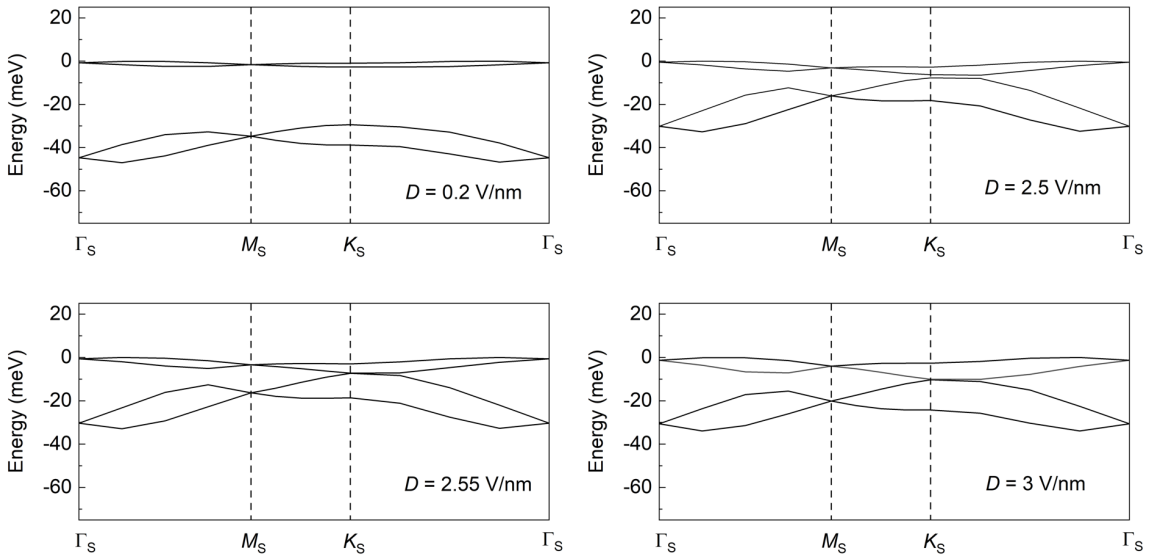

Supplementary Figure S9. DFT band structures at varying displacement fields. Electronic band structure (first two hole moiré bands) of zero-degree-aligned $MoTe_2/WSe_2$ heterobilayers from DFT under displacement field D = 0.2 V/nm, 2.5 V/nm, 2.55 V/nm and 3.0 V/nm.

8. Effects of bias voltage

Supplementary Fig. S10a shows the differential resistance $\frac{dV}{dI}$ versus bias voltage V at 350 mK under several electric fields on the metallic side. It stays flat for bias voltage up to 4-5 mV for all the applied electric fields. Supplementary Fig. S10b shows the resistance across the MIT measured with three different bias voltages, 1 mV, 2 mV, and 5 mV. The I-V characteristic becomes nonlinear when the sample is very insulating; the measured resistance drops at large bias values. This presumably is caused by sample heating at high biases. In our measurements, we have kept the bias voltage at 1 mV to be safely in the linear regime for all electric fields and temperatures. Furthermore, the activation gap on the insulating side is extracted from the high-temperature data; the sample resistance is much smaller and the I-V curves are linear over a much wider range of bias voltages (Supplementary Fig. S11).

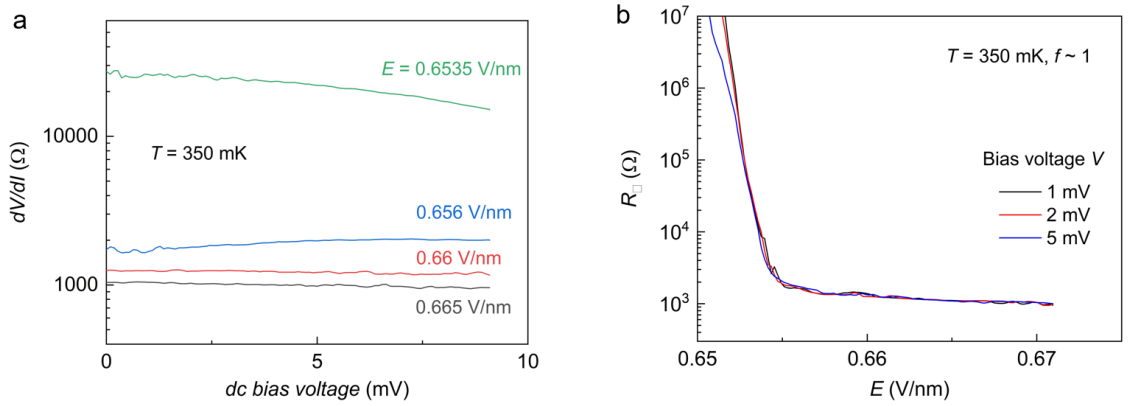

Supplementary Figure S10. Bias dependent sample resistance at 350 mK. a, Bias voltage (V) dependence of the $f = 1$ differential resistance, $\frac{dV}{dI}$, at 350 mK under varying vertical electric fields on the metallic side. The ac modulation voltage is 0.5 mV. The differential resistance is independent of V for $V \lesssim 4-5$ mV. **b,** Electric-field dependence of square resistance measured at three different bias voltages at 350 mK. The resistance drops slightly on the insulating side at 5 mV bias likely due to heating at high biases.

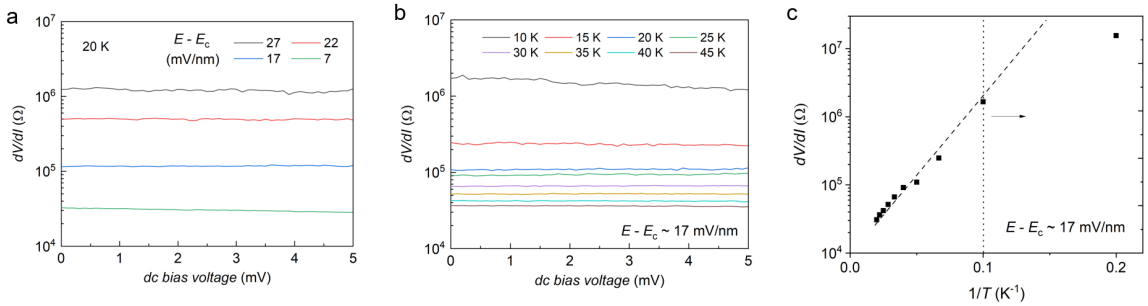

Supplementary Figure S11. Bias dependence of the sample resistance at $f = 1$ on the insulating side (data from another device). a, Differential resistance, $\frac{dV}{dI}$, as a function of DC bias voltage (V) at 20 K under varying vertical electric fields. The AC

modulation voltage is 0.5 mV. The differential resistance is approximately bias independent for bias up to 5 mV. **b,** Same as in **a** for a fixed electric field (17 mV/nm from the critical point) at varying temperatures. The differential resistance is approximately bias independent down to 10 K for bias below 1-1.5. **c,** Arrhenius plot of the square resistance at $V = 1$ mV. Thermal activation behavior is seen above ~ 10 K. The vertical dotted line indicates an onset of nonlinear I-V dependence observed at bias V = 5 mV.

9. Extracted contact resistance

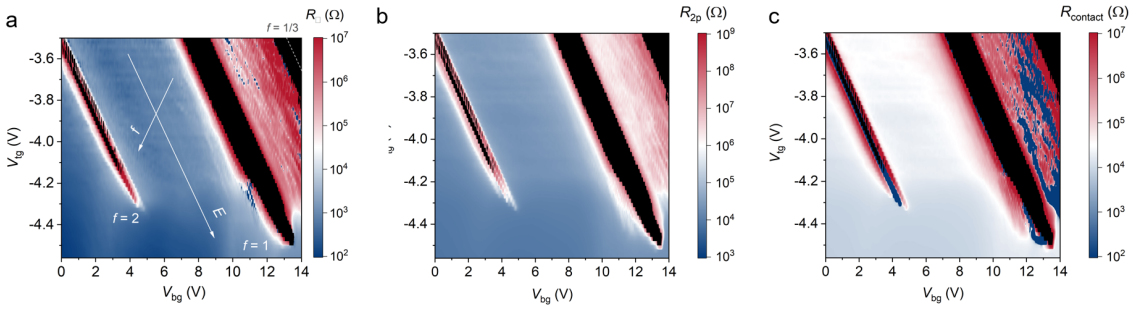

Supplementary Figure S12. Square resistance, 2-point resistance and contact resistance. 2D map of the top and bottom gate voltage dependences of the square resistance (**a**), 2-point source-drain resistance (**b**) and the estimated contact resistance (**c**) from the difference between **b** and **a** at 300 mK. The estimated resistance in **c** also includes the sample inhomogeneity effect, particularly, in the region near the insulating states. The contact resistance drops substantially at large filling factors and high electric fields. The contact resistance exceeds 10 MΩ for $f < 1$ for most of the electric fields.

Supplementary References

1. Tang, Y., Gu, J., Liu, S., Watanabe, K., Taniguchi, T., Hone, J., Mak, K.F. & Shan, J. Tuning layer-hybridized moiré excitons by the quantum-confined Stark effect. *Nature Nanotechnology* **16**, 52-57 (2021).
2. Li, T., Zhu, J., Tang, Y., Watanabe, K., Taniguchi, T., Elser, V., Shan, J. & Mak, K.F. Charge-order-enhanced capacitance in semiconductor moir\'e superlattices. *arXiv preprint arXiv:2102.10823* (2021).
3. Regan, E.C., Wang, D., Jin, C., Bakti Utama, M.I., Gao, B., Wei, X., Zhao, S., Zhao, W., Zhang, Z., Yumigeta, K., Blei, M., Carlström, J.D., Watanabe, K., Taniguchi, T., Tongay, S., Crommie, M., Zettl, A. & Wang, F. Mott and generalized Wigner crystal states in WSe2/WS2 moiré superlattices. *Nature* **579**, 359-363 (2020).
4. Xu, Y., Liu, S., Rhodes, D.A., Watanabe, K., Taniguchi, T., Hone, J., Elser, V., Mak, K.F. & Shan, J. Correlated insulating states at fractional fillings of moiré superlattices. *Nature* **587**, 214-218 (2020).
5. Wu, F., Lovorn, T., Tutuc, E. & MacDonald, A.H. Hubbard Model Physics in Transition Metal Dichalcogenide Moire Bands. *Physical Review Letters* **121**, 026402 (2018).

6. Zhang, F.C. & Rice, T.M. Effective Hamiltonian for the superconducting Cu oxides. *Physical Review B* **37**, 3759-3761 (1988).
7. Zhang, Y., Yuan, N.F.Q. & Fu, L. Moire quantum chemistry: Charge transfer in transition metal dichalcogenide superlattices. *Physical Review B* **102**, 201115 (2020).
8. Lee, P.A., Nagaosa, N. & Wen, X.-G. Doping a Mott insulator: Physics of high-temperature superconductivity. *Reviews of Modern Physics* **78**, 17-85 (2006).
9. Srivastava, A., Sidler, M., Allain, A.V., Lembke, D.S., Kis, A. & Imamoğlu, A. Valley Zeeman effect in elementary optical excitations of monolayer WSe2. *Nature Physics* **11**, 141-147 (2015).
10. Tang, Y., Li, L., Li, T., Xu, Y., Liu, S., Barmak, K., Watanabe, K., Taniguchi, T., MacDonald, A.H. & Shan, J. Simulation of Hubbard model physics in WSe 2/WS 2 moiré superlattices. *Nature* **579**, 353-358 (2020).